Hindawi
Advances in Mathematical Physics
Volume 2021, Article ID 7519141, 9 pages
https://doi.org/10.1155/2021/7519141

Research Article

Effect of Scraper Geometry on Scraping HAP/ZrO_2 Slurry in Digital Light Processing

Hai Gu,[1,2,3] **Jie Zhang**,[1,2,3] **Jianhua Sun**,[1] **Tiancheng Huang**,[2] **Jie Jiang**,[1,2] **Bin Li**,[1,2,3] **and Weiwei Wu**[4]

[1]*School of Mechanical Engineering, Nantong Institute of Technology, Nantong 226002, China*
[2]*Jiangsu Key Laboratory of 3D Printing Equipment and Application Technology, Nantong Institute of Technology, Nantong 226002, China*
[3]*Department of IT Engineering, Mokwon University, Daejeon 35349, Republic of Korea*
[4]*School of Mechanical Engineering, Yangzhou University, Yangzhou 225127, China*

Correspondence should be addressed to Hai Gu; guhainit@163.com

Received 1 September 2021; Accepted 25 November 2021; Published 20 December 2021

Academic Editor: Shuo Yin

Copyright © 2021 Hai Gu et al. This is an open access article distributed under the Creative Commons Attribution License, which permits unrestricted use, distribution, and reproduction in any medium, provided the original work is properly cited.

Digital light processing (DLP) can be used to form HAP/ZrO_2 mixed ceramic slurry. In the printing technology, the scraper geometry has an important effect on the scraping process; thus, it is necessary to conduct analysis. A modified lattice Boltzmann method (LBM) is proposed to conduct the numerical simulations according to the non-Newtonian behavior of the slurry. The Cross behavior of the slurry is viewed as a special external force; then, the traditional LBM including the true external force can be utilized effectively. The triangle, rectangle, trapezium, and rounded rectangle are the main considered section geometries of the scraper. When the flow velocity is set to 0.1 m/s, the results show that the maximum velocity occurs near the bottom surface of the scraper. In four situations, the velocity peak of the triangle case is 0.6270 m/s, which is the maximum, and much larger than the flow velocity of 0.1 m/s. The velocity peak of the rectangle case is 0.0466 m/s, which is the minimum. Although the velocity peak of the rounded rectangle case is 0.0556 m/s, the second velocity peak is 0.0465 m/s; the difference is smaller than that of the rectangle case. In addition, the streamlines figures show that the sharp corner leads to the obvious velocity change. In summary, the rounded rectangle is considered to be more suitable for scraping the HAP/ZrO_2 mixed slurry.

1. Introduction

Digital light processing (DLP), an additive manufacturing (AM) technology, can process photosensitive resin materials accurately [1–4]. In recent years, a mixture of resins and other materials are developed for printing [4–6]. With traditional technology, some materials (such as ceramic materials) are difficult to machine freely. DLP or similar AM technology provides an effective method to mold ceramic parts [7–11].

The general DLP molding process for ceramic material includes several parts as follows. (1) *Slurry preparation*. The slurry is obtained by mixing the resins, the ceramic powders, and some essential additives with a proper proportion. In general, high solid content and low viscosity are recommended for successful printing. (2) *Printing*. According to the graphic information obtained from the 3D software, the slurry is solidified layer by layer. When a layer is printed, the printing bench is moved up or down with a distance of thickness, a new layer slurry covers the last layer, and a scraper is moved forward to make the surface smooth and compact. The application of this process is based on an array of micromirrors suitable for orientation into two positions, moved by microactuators. The UV light is reflected by these micromirrors to the layer of the liquid photopolymer, placed in a tank. Depending on the orientation of the micromirror, each pixel of material is cured or not. The resolution of the cured mask is defined by the number of pixels [2] (Figure 1). (3) *Debinding and sintering*. When finishing the printing, the degreasing and sintering steps are required to

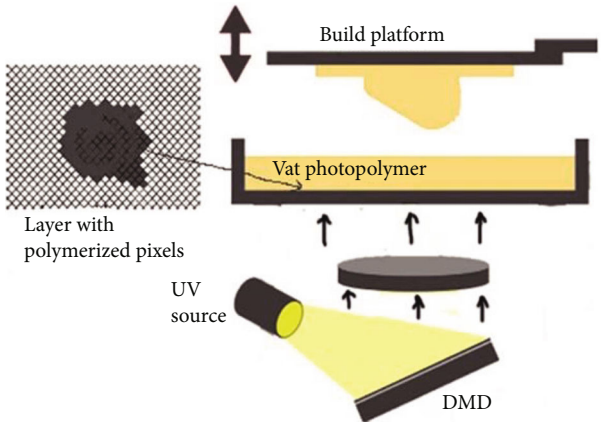

Figure 1: Digital light processing method [2].

improve the density and mechanical performances. It is noted that a smoother and compacter layer contributes to better accuracy. Thus, suitable scraper geometry is crucial.

In the work, the ceramic material involved is HAP/ZrO_2. The purpose is to select a proper scraper geometry for DLP technology. Most of the studies focus on the material formula [12, 13] and technology optimization [14, 15], while the research on the scraper process is still relatively weak. The problem belongs to fluid analysis, and the main analysis methods include experiments and numerical simulations. Regarding the experiments, the sensors are always required, which are sensitive to the environmental parameters (temperature, pressure, and humidity, etc.). It is not suitable here for the analysis. When referring to the numerical simulations, the common methods include commercial software (such as Fluent and Polyflow) and programming method (such as LBM and molecular dynamics method). Fluent is the most frequently used software, which can solve many engineering problems [16–18]. However, the fluid flow in many fields is complex [19–21], especially some fluids that exhibit complicated non-Newtonian behavior, and secondary development is always required. In the present work, the HAP/ZrO_2 slurry presents typical non-Newtonian behavior. When using Fluent, the divergence may occur in the simulation process. Thus, the programming method lattice Boltzmann method (LBM) is selected here to conduct the simulations. As a mesoscopic method, it has been widely used in many engineering areas, such as mechanical engineering, bioengineering, and engineering thermal physics. It can also be used to solve non-Newtonian problems. Yoshino et al. proposed a modified LBM for incompressible non-Newtonian fluid flows, and a variable parameter is used to describe the viscosity by using the local shear rate [22]. Psihogios et al. used LBM to analyze non-Newtonian shear-thinning (power-law) fluids in three-dimensional porous media [23]. Di Ilio et al. conducted numerical simulations to investigate the incompressible laminar power-law flow in symmetric channel with sudden expansion, and the ability of LBM for solving the flow is explored in detail [24]. Bisht and Patil used LBM with multiple relaxation time collisions to assess the non-Newtonian flow for benchmarks configurations [25]. Gokhale and Fernandes studied forced convection in Carreau-Yasuda fluids flowing through sandstones based on LBM for both shear-thinning and shear-thickening fluids [26].

Though many studies have been done on the non-Newtonian fluids, the viscosity changes with the shear rate, which may result in instability in the simulation process. Thus, modified methods are always required to improve stability or accuracy. Conrad et al. proposed a viscosity adaption method for LBM to analyze non-Newtonian fluids, whose effectiveness is also validated [27], which is much more complex and difficult to achieve by programming. Gabbanelli et al. presented a truncated LBM for power-law fluids, which is validated by several classical cases [28]. Wu et al. proposed a truncated multiple relaxation time LBM for Herschel-Bulkley flow with a high Reynolds number and the feasibility of the modified method is validated by the known cases [29]. The truncated method requires calculating the truncated points for each case, and the obvious error exists in the transform process, especially for the fluids including yielding behavior. Zou et al. incorporated LBM into the finite volume method (FVM) to simulate viscoelastic fluid flows [30], which is difficult to achieve. Li et al. presented an immersed boundary LBM to simulate power-law nanofluid flow in a square enclosure [31], which mainly focuses on boundary processing, while the main method is still the standard LBM.

The prepared HAP/ZrO2 slurry is a kind of non-Newtonian fluid. To improve the stability and/or accuracy of the simulation, the modification of the standard LBM is also required. The Cross behavior is viewed as a special external force item; then, the traditional LBM including true external force can be utilized effectively. When compared with the above-modified methods in the literature, the proposed modified LBM in the study is easy to achieve by programming and suitable for many kinds of non-Newtonian fluids.

The remainder of this paper is organized as follows. Section 2 conducts the rheological test of HAP/ZrO_2 mixed slurry. Section 3 outlines the improved LBM. The Cross behavior is viewed as a special external force item. Then, the necessary simulations for four cases are conducted. In Sections 4 and 5, the discussion and conclusion are summarized.

2. Rheological Test

2.1. Material Preparation. The required materials include nanohydroxyapatite (HAP) powders, nanozirconia (ZrO_2) powders, polyethylene glycol diacrylate (PEGDA), ethylene glycol dimethacrylate (EGDMA), polyester acrylic resin, propyl trimethoxysilane (KH-570), and 2,4,6-trimethylbenzoylphenylphosphonate ethyl (TPO-L).

(1) *Modifying HAP with KH-570.* Add ethanol, KH-570, and acidified distilled water with a proportion of 10 : 1 : 5 into a beaker, then hydrolyze at 25°C for 4 h and remove the water layer. Add HAP powders (5%) and ethanol into a flask with three necks, add KH-570 during the heating process, and conduct

suction filtration after reaction at 60°C for 14 h. Dry the powders in the circulation oven at 50°C

(2) *Preparing resin*. Mix PEGDA, EGDMA, and a polyester acrylic resin with a certain weight proportion of 2 : 2 : 1 by use of magnetic stirring for 40 min

(3) *Preparing slurry*. Mix modified HAP powders (60 wt%), nano-ZrO_2 powders (1-6 wt%), and TPO-L (0.6 wt%), then conduct mechanical stirring at 800-1300 rpm for 4 h

2.2. Rheological Equation. To understand the rheological behavior, the obtained HAP/ZrO_2 (ZrO_2 powders are added with 1 wt%, 3 wt%, and 6 wt%, respectively) slurry is measured by an AR2000 EX rheometer. The shear rate is increased from 0.1 to 1000 s^{-1}, and the corresponding viscosities are measured and recorded as shown in Figure 2. The viscosity decreases with increasing the shear rate, and the slurry presents typical non-Newtonian behavior.

To facilitate the fluid analysis, it is necessary to obtain the specific rheological equation of HAP/ZrO_2 slurry. By using Curve Fitting toolbox in MATLAB 2014b software, the common non-Newtonian equations are selected for fitting, and the result shows that the Cross model can well match with the experimental data. The correlation coefficient R^2 is 0.9995, which is very close to 1. The specific model is shown as follows:

$$\mu = \frac{\mu_0}{1 + (\lambda\dot{\gamma})^{1-n}} \Rightarrow \mu = \frac{50.04}{1 + (41.79\dot{\gamma})^{0.97319}}. \quad (1)$$

3. Analysis of Scraper Geometries

3.1. LBM for HAP/ZrO_2 Slurry. To solve the instability and/or inaccuracy of non-Newtonian slurry, the standard lattice Boltzmann method is always required to modify. An improved LBM is proposed for the Cross model as below. Guo et al. proposes the lattice Boltzmann equation with an external force as follows [32]:

$$\boldsymbol{f}(\boldsymbol{r} + \boldsymbol{e_i}\delta t, t + \delta t) - \boldsymbol{f}(\boldsymbol{r}, t) = -\frac{1}{\tau}[\boldsymbol{f}(\boldsymbol{r}, t) - \boldsymbol{f}^{\boldsymbol{eq}}(\boldsymbol{r}, t)] + \delta t\boldsymbol{F}', \quad (2)$$

where $\boldsymbol{r}$ is the displacement vector and τ is the relaxation time; the discrete velocity $\boldsymbol{e_i}$ is expressed as follows:

$$\boldsymbol{e}_i = \begin{cases} (0, 0), & i = 0, \\ c\left(\cos\dfrac{i-1}{2}\pi, \sin\dfrac{i-1}{2}\pi\right), & i = 1, 2, 3, 4, \\ \sqrt{2}c\left(\cos\dfrac{2i-9}{4}\pi, \sin\dfrac{2i-9}{4}\pi\right), & i = 5, 6, 7, 8, \end{cases} \quad (3)$$

where δx and δt are the lattice step size and time step size, respectively, both of which are always set to 1. The lattice speed is $c = \delta x/\delta t$. $\boldsymbol{f}$ and $\boldsymbol{f}^{\boldsymbol{eq}}$ correspond to the general and equilibrium distribution functions; the latter is described as follows:

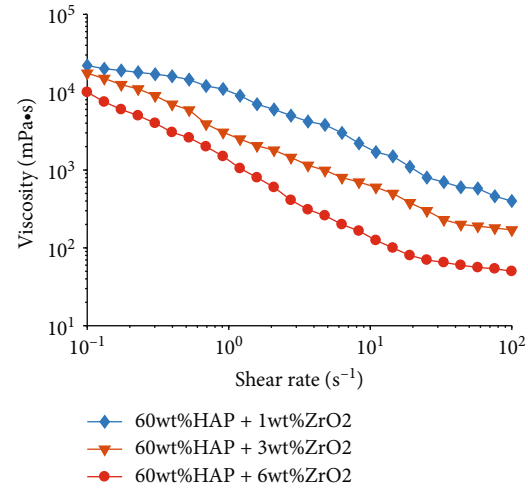

FIGURE 2: Rheological test data.

$$\boldsymbol{f}^{\boldsymbol{eq}}(\boldsymbol{r}, t) = \omega_i\rho\left[1 + \frac{\boldsymbol{e_i}\cdot\boldsymbol{u}}{c_s^2} + \frac{(\boldsymbol{e_i}\cdot\boldsymbol{u})^2}{2c_s^4} - \frac{\boldsymbol{u}^2}{2c_s^2}\right], \quad (4)$$

where c_s, given by $c_s^2 = c^2/3$, is the lattice sound speed, $\boldsymbol{u}$ is the velocity vector, and ω_i, given by $\omega_0 = 4/9$ for $i = 0$, $\omega_i = 1/9$ for $i = 1 - 4$, and $\omega_i = 1/36$ for $i = 5 - 8$, is the weight coefficient.

It is noted that two steps are included in Equation (2) as collision and streaming. The specific equation for the collision step is

$$\boldsymbol{f}^{+}(\boldsymbol{r}, t) = \boldsymbol{f}(\boldsymbol{r}, t) + \frac{1}{\tau}[\boldsymbol{f}(\boldsymbol{r}, t) - \boldsymbol{f}^{\boldsymbol{eq}}(\boldsymbol{r}, t)] + \delta t\boldsymbol{F}', \quad (5)$$

where $\boldsymbol{F}'$ is the external force, which is described as

$$\boldsymbol{F}_i' = \omega_i\left(1 - \frac{\delta t}{\tau}\right)\left[\frac{\boldsymbol{e_i} - \boldsymbol{u}}{c_s^2} + \frac{(\boldsymbol{e_i}\cdot\boldsymbol{u})}{c_s^4}\cdot\boldsymbol{e_i}\right]\bar{\boldsymbol{F}}. \quad (6)$$

The specific equation for the streaming step is

$$\boldsymbol{f}(\boldsymbol{r} + \boldsymbol{e_i}\delta t, t + \delta t) = \boldsymbol{f}^{+}(\boldsymbol{r}, t). \quad (7)$$

The strain rate tensor for HAP/ZrO_2 slurry is expressed as follows:

$$\boldsymbol{S}_{\alpha\beta} = -\frac{1}{2\rho\tau c_s^2}\sum_{i=0}^{8}\boldsymbol{e}_{i\alpha}\boldsymbol{e}_{i\beta}(\boldsymbol{f}_i - \boldsymbol{f}_i^{eq}), \quad (8)$$

where ρ is density.

Then, the second invariant of strain rate tensor can be calculated with $\boldsymbol{S}_{\alpha\beta}$ as follows:

$$D_{II} = \sum_{\alpha,\beta=1}^{l} \boldsymbol{S}_{\alpha\beta}\boldsymbol{S}_{\alpha\beta}. \tag{9}$$

Therefore, the shear rate can be obtained as follows:

$$\dot{\gamma} = \sqrt{2D_{II}}. \tag{10}$$

According to the isotropic constraint condition, we can obtain

$$\sum_{i=1}^{9} \boldsymbol{f}_i^{eq}\mathbf{e}_{i\alpha}\mathbf{e}_{i\beta} = \rho u_\alpha u_\beta + P\delta_{\alpha\beta} = \rho u_\alpha u_\beta + \frac{1}{3}\rho\delta_{\alpha\beta}, \tag{11}$$

where $\delta_{\alpha\beta}$ is the Kronecker delta. Furthermore, the distribution function and momentum flux tensor can be expanded by the Champan-Enskog expansion as

$$\boldsymbol{f}_i \approx \boldsymbol{f}_i^{eq} + \varepsilon\boldsymbol{f}_i^{(1)} + \varepsilon^2\boldsymbol{f}_i^{(2)}, \tag{12}$$

$$\prod_{\alpha\beta} \approx \overset{(0)}{\prod_{\alpha\beta}} + \overset{(1)}{\prod_{\alpha\beta}}. \tag{13}$$

By solving the first moment of the velocity, the equilibrium and nonequilibrium momentum flux tensors $\prod_{\alpha\beta}^{(0)}$ and $\prod_{\alpha\beta}^{(1)}$ are expressed as

$$\overset{(0)}{\prod_{\alpha\beta}} = \sum_i e_{i\alpha}e_{i\beta}\boldsymbol{f}_i^{eq} = P\delta_{\alpha\beta} + \rho u_\alpha u_\beta, \tag{14}$$

$$\overset{(1)}{\prod_{\alpha\beta}} = \sum_{i=1}^{9} e_{i\alpha}e_{i\beta}\left(1 - \frac{1}{2\tau}\right)\boldsymbol{f}_i^{(1)}. \tag{15}$$

Thus, by Equations (13)–(15), the momentum flux tensor can be expressed as

$$\prod_{\alpha\beta} = P\delta_{\alpha\beta} + \rho u_\alpha u_\beta - 2\mu\boldsymbol{S}_{\boldsymbol{\alpha\beta}}, \tag{16}$$

where μ is the dynamic viscosity of Cross fluids. The relaxation time τ can be calculated by

$$\mu = \rho c_s^2\left(\tau - \frac{1}{2}\right)\delta t. \tag{17}$$

There is another expression for the momentum flux tensor of the incompressible fluid as

$$\prod_{\alpha\beta} = \rho u_\alpha u_\beta - \sigma_{\alpha\beta}. \tag{18}$$

The stress tensor $\sigma_{\alpha\beta}$ can be further calculated according to Equations (14), (16), and (18).

$$\sigma_{\alpha\beta} = -P\delta_{\alpha\beta} + \frac{2\mu_0}{1 + (\lambda\dot{\gamma})^{1-n}}\boldsymbol{S}_{\boldsymbol{\alpha\beta}}. \tag{19}$$

With the expansion of Chapman-Enskog, the Navier-Stokes equation at the incompressible limit can be recovered as follows:

$$\begin{aligned}\rho\partial_t(u_\beta) + (\rho u_\alpha)\partial_\alpha u_\beta &= -\partial_\beta P + 2\mu_0\partial_\alpha\boldsymbol{S}_{\boldsymbol{\alpha\beta}} - \frac{2\mu_0(\lambda\dot{\gamma})^{1-n}}{1 + (\lambda\dot{\gamma})^{1-n}}\partial_\alpha\boldsymbol{S}_{\boldsymbol{\alpha\beta}} \\ &= -\partial_\beta P + 2\mu_0\partial_\alpha\boldsymbol{S}_{\boldsymbol{\alpha\beta}} + \bar{\boldsymbol{F}}.\end{aligned} \tag{20}$$

Thus, the specific equation for $\bar{\boldsymbol{F}}$ is as follows:

$$\bar{\boldsymbol{F}} = -\frac{2\mu_0(\lambda\dot{\gamma})^{1-n}}{1 + (\lambda\dot{\gamma})^{1-n}}\partial_\alpha\boldsymbol{S}_{\boldsymbol{\alpha\beta}}. \tag{21}$$

Combine Equations (7) and (21), the discrete force term can be obtained as follows:

$$\boldsymbol{F}_{\boldsymbol{i}}' = -\frac{2\mu_0(\lambda\dot{\gamma})^{1-n}}{1 + (\lambda\dot{\gamma})^{1-n}}\omega_i\left(1 - \frac{\delta t}{\tau}\right)\left[\frac{\boldsymbol{e}_i - \boldsymbol{u}}{c_s^2} + \frac{(\boldsymbol{e}_i\cdot\boldsymbol{u})}{c_s^4}\cdot\boldsymbol{e}_i\right]\partial_\alpha S_{\alpha\beta}. \tag{22}$$

3.2. Validation. Regarding the equation of the Cross model in Equation (1), when $\lambda = n = 1$, the Cross fluid changes into the Newtonian fluid. The Poiseuille flow (Figure 3) for Newtonian fluid has the theoretical solution, which can be used to validate the effectiveness of the proposed method. The specific result of Poiseuille flow is expressed as follows:

$$u(y) = \frac{1}{2}\left(-\frac{1}{\mu_{N0}}\frac{\partial p}{\partial x}\right)\left[\left(\frac{H}{2}\right)^2 - |y|^2\right]. \tag{23}$$

The relevant parameters are set as follows. The viscosity μ_{N0} is 0.1, the pressure gradient $\partial p/\partial x$ is -1×10^{-3}, the distance between two plates H is 1, and the lattice numbers are 100×100. The comparison between the theoretical and numerical solutions shown in Figure 4 is coincident, which validates the feasibility of the modified LBM for the HAP/ZrO_2 slurry flow.

3.3. Simulation of the Flow with Different Scraper Geometries

3.3.1. Simulation Preparation. During the printing process, a new layer should be laid from the right to the left by a scraper after finishing one layer. To obtain a compact and even layer, it is important to select the proper geometry for the scraper. As shown in Figure 5, four different scrapers are designed. Under the assumption that the scraper is still, then the slurry flows through the scraper from left to right.

The specific parameters are set as follows. The width of the scraper W is 6 mm, the layer thickness H is 0.5 mm,

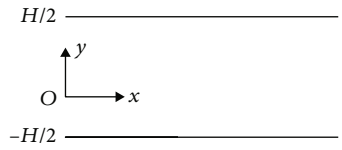

Figure 3: Poiseuille flow.

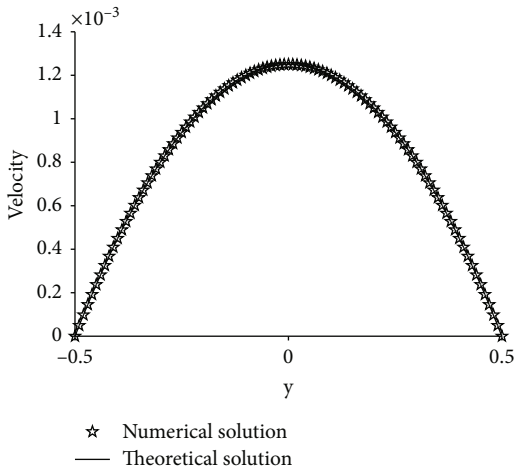

Figure 4: Comparison between numerical and theoretical solutions.

the distance between the blade and printed layer h is 0.05 mm, the angle θ in the first figure is $\pi/4$, the angle γ in the third figure is $3\pi/4$, the bottom width in the third figure is 2 mm, and the radius r in the fourth figure is 2 mm. In addition, the flow velocity is set as 0.1 m/s. The layering length discussed here is 15 mm.

In the simulation, the dimensionless lattice parameters are set as follows. The lattice numbers are 25×750, and the velocity is 0.01. The rheological parameters can be obtained from Equation (1), such as the viscosity coefficient, and the power-law index. The Reynolds number is selected as the criterion parameter; therefore, the physical Reynolds number should be equal to the lattice calculation. According to the proposed method, the streamlines and velocity distribution can be figured. The streamlines can reveal the flow track of the slurry, and the cloud atlas can present the magnitude of the flow velocity. The blue color zone indicates the low-velocity area, and the yellow color zone illustrates the high-velocity area. In addition, the curve of the velocity distribution describes the magnitude of the velocity in detail. Regarding the proper geometry of the scraper, the following points should be satisfied to obtain the smooth layering: (1) The horizontal velocity at the back of the scraper is low enough, and the sudden change of the velocity should be avoided. (2) The angle between the maximum vertical velocity and the horizontal direction is expected to be small.

The simulation is conducted by using the program in MATLAB 2014b software. The specific procedures are given in Figure 6.

3.3.2. Simulation Results. In the first situation, the section of the scraper is a triangle. The streamlines are shown in Figure 7(a), which implies that the phenomenon of jet expansion occurs near the vertex of the scraper. The high velocity shown as the yellow zone is concentrated below the scraper. In Figure 7(b), the high-velocity distribution is given, where the blue and red curves correspond to the velocity at the height of 0.46 mm and 0.48 mm, respectively, which shows that the maximum velocity is 0.6270 m/s, and the corresponding point is very close to the back of the scraper. In addition, the angle between the maximum vertical velocity and the horizontal direction is 67.2°.

The second considered geometry of the section is the rectangle. The simulation results are shown in Figure 8, which implies that the vertical velocity at the lower-right point is close to the back of the scraper. The angle between the vertical velocity and the horizontal direction is 74.4°. The velocity distribution in Figure 8(b) presents that there is a sudden change at the back of the scraper. When compared with the triangle situation, the maximum velocity is much lower.

Then, the trapezium section geometry is considered. The high velocity is below the scraper as shown in Figure 9(a). In Figure 9(b), the velocity distribution shows that the maximum velocity occurs at $x = 8.5$ mm, which corresponds to the right point of the bottom edge. The angle between the maximum vertical velocity and the horizontal direction is 43.7°. When compared with the above two cases, the point of the maximum horizontal velocity occurs at the left of the back edge, and the mentioned angle is smaller.

The bottom corners are changed into arcs based on the second situation. The simulation results are shown in Figure 10. The velocity distribution in Figure 10(b) implies that the maximum horizontal velocity is 0.0556 m/s, which occurs at $x = 8.68$ mm. The streamlines show a gradual change in velocity. The angle between the maximum vertical velocity and the horizontal direction is 10.5°.

4. Discussion

The layering process has an important effect on the printing performance in DLP technology. The material studied here is HAP/ZrO_2. According to the rheological test, the ceramic slurry presents typical non-Newtonian behavior. In the printing process, the smooth layering is always recommended; it is necessary to investigate the effect of the geometry of the scraper on layering. With the consideration of the general geometries of the scrapers, four different situations are explored and simulated by an improved LBM. The high velocity at the back of the scraper should be avoided, and the maximum horizontal velocity is expected to be far from the back of the scraper. In addition, the streamlines show that the jet expansion occurs near the back, which results in the appearance of vertical velocity. It is suggested that the slope of the vertical velocity should be small.

In the first case, the section is triangle geometry. The maximum horizontal velocity occurs at the back of the scraper, which interferes with the layered materials and is not in favor of the layering process. In the second case, the sudden change of the horizontal velocity occurs at the back edge, which generates turbulence at the surface of the

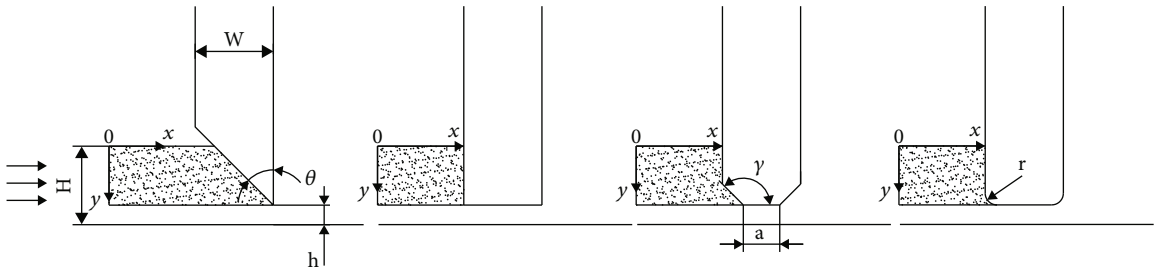

Figure 5: Four situations of the scrapers.

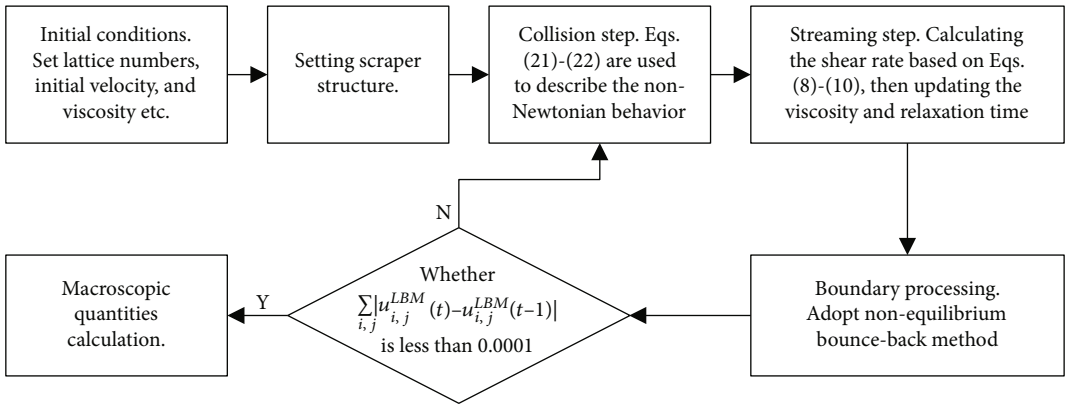

Figure 6: Flow chart of the simulation.

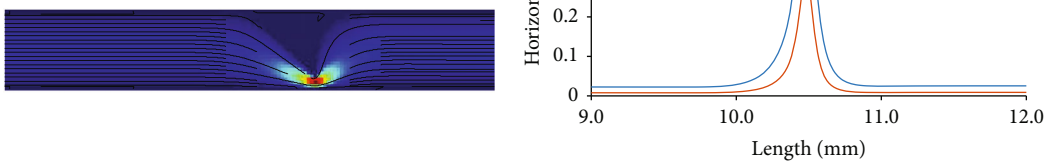

(a) Streamlines of the flow (b) Horizontal velocity distribution below the scraper

Figure 7: Simulation result of the first situation.

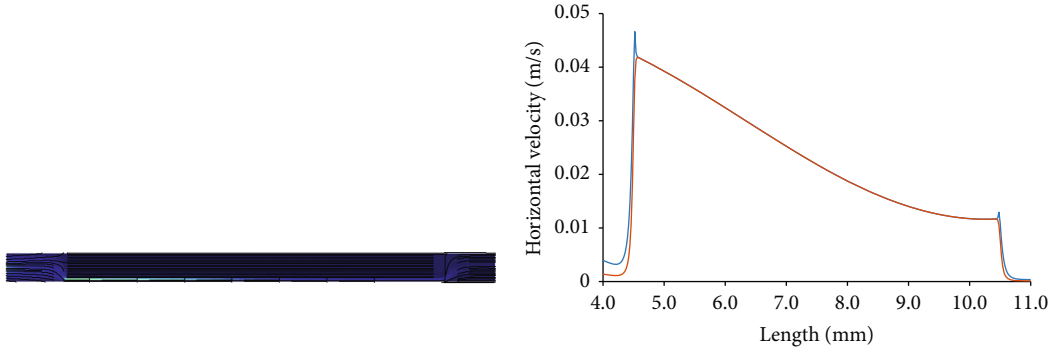

(a) Streamlines of the flow (b) Horizontal velocity distribution below the scraper

Figure 8: Simulation result of the second situation.

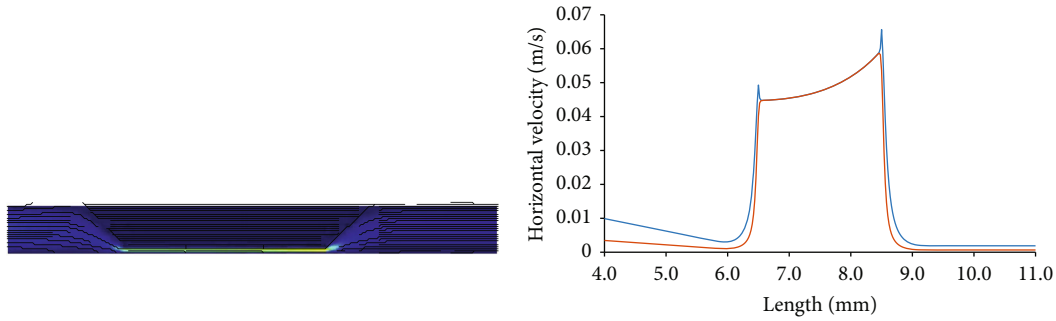

(a) Streamlines of the flow (b) Horizontal velocity distribution below the scraper

Figure 9: Simulation result of the third situation.

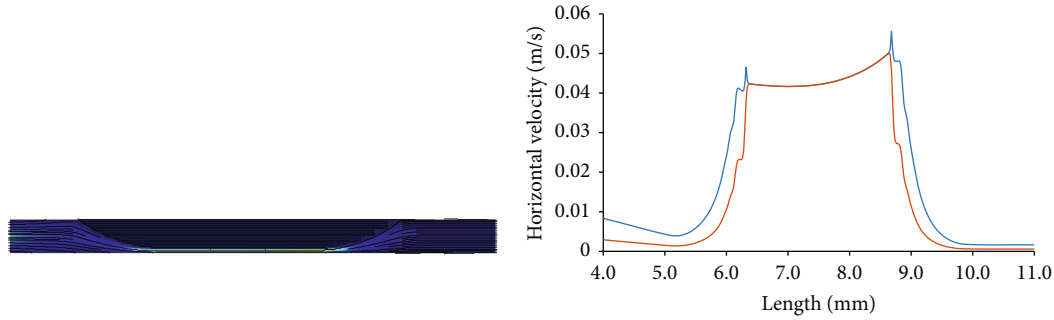

(a) Streamlines of the flow (b) Horizontal velocity distribution below the scraper

Figure 10: Simulation result of the fourth situation.

Table 1: Comparison of the velocity results for four cases.

	First velocity peak (m/s)	Second velocity peak (m/s)	Difference (m/s)
Triangle case	0.6270	—	—
Rectangle case	0.0466	0.0129	0.0337
Trapezium case	0.0657	0.0493	0.0164
Rounded rectangle case	0.0556	0.0465	0.0091

smooth layer. Both in the third and fourth cases, the point of the maximum horizontal velocity keeps a certain distance from the back edge, and the sudden decrease of the velocity also does not appear near the back edge.

Then, the angle between the maximum vertical velocity and the horizontal direction should be also considered. According to the results, the mentioned angles for the four cases are 67.2°, 74.4°, 43.7°, and 10.5°. The last case presents a much smaller angle than the other cases, which means the jet expansion is much flatter. According to the above two points, the last case is considered to be the most suitable for the layering process.

5. Conclusion

As a new technology, DLP provides an effective method for molding ceramic parts. In the present work, HAP/ZrO_2 powders are used in DLP technology. The Cross model of the slurry is measured and built; then, a modified LBM is proposed to improve the stability of the numerical simulation which may be caused by the non-Newtonian behavior. The purpose of the work is to analyze the geometry of the scraper on the layering process and determine the suitable geometry. The key velocities are listed in Table 1, which shows that the rectangle case has the minimum first velocity peak; however, the difference between the first and the second velocity peak is larger than that between the trapezium and rounded rectangle cases. After a general comparison among these cases, the velocity of the rounded rectangle case is the best.

Thus, the proper geometry is that the section of the scraper is a rounded rectangle. In this situation, the jet expansion is weak, and the point of the maximum horizontal velocity is far from the back edge, which does not affect the layered slurry. The sudden change of velocity is also avoided. In the following research, the different ceramic materials will be further investigated to validate the effectiveness of the rounded rectangle geometry of the scraper.

Data Availability

The data that support the findings of this study are available from the corresponding author upon reasonable request.

Conflicts of Interest

The authors have no conflicts to disclose.

Acknowledgments

This work was financially supported by the Top Talent Project of Nantong Institute of Technology (XBJRC2021003), Key University Science Research Project of Jiangsu Province (Grant No. 18KJA460006), Top-Notch Academic Programs Project of Jiangsu Higher Education Institutions (Grant No. 2020-9), Key R&D Plan of Jiangsu Province (Grant Nos. BE2018010-4 and BY2020545), Science and Technology Project of Nantong (Grant Nos. JC2020155, JCZ19122, JCZ20056, and JC2020132), Key Laboratory of Laser Processing and Metal Additive of Provincial Science and Technology Service Platform Cultivation Project of Nantong Institute of Technology (Grant No. XQPT202101), and Natural Science Foundation of the Jiangsu Higher Education Institutions of China (Grant No. 21KJD460005).

References

[1] İ. Ertuğrul, "The fabrication of micro beam from photopolymer by digital light processing 3D printing technology," *Micromachines*, vol. 11, no. 5, p. 518, 2020.

[2] M. Monzón, Z. Ortega, A. Hernández, R. Paz, and F. Ortega, "Anisotropy of photopolymer parts made by digital light processing," *Materials*, vol. 10, no. 1, p. 64, 2017.

[3] C. Feng, K. Zhang, R. He et al., "Additive manufacturing of hydroxyapatite bioceramic scaffolds: dispersion, digital light processing, sintering, mechanical properties, and biocompatibility," *Journal of Advanced Ceramics*, vol. 9, no. 3, pp. 360–373, 2020.

[4] Z. Mei, Y. Lu, Y. Lou et al., "Determination of hardness and fracture toughness of Y-TZP manufactured by digital light processing through the indentation technique," *Bio Med Research International*, vol. 2021, pp. 1–11, 2021.

[5] H. Han and S. Cho, "Fabrication of conducting polyacrylate resin solution with polyaniline nanofiber and graphene for conductive 3D printing application," *Polymers*, vol. 10, no. 9, p. 1003, 2018.

[6] C. F. Li, X. Kuang, A. Mulyadi, C. M. Hamel, Y. Deng, and H. J. Qi, "3D printed cellulose nanocrystal composites through digital light processing," *Cellulose*, vol. 26, no. 6, pp. 3973–3985, 2019.

[7] D. Shin and J. Hyun, "Silk fibroin microneedles fabricated by digital light processing 3D printing," *Journal of Industrial and Engineering Chemistry*, vol. 95, pp. 126–133, 2021.

[8] K. Zhang, R. He, G. Ding, C. Feng, W. Song, and D. Fang, "Digital light processing of 3Y-TZP strengthened ZrO_2 ceramics," *Materials Science and Engineering A*, vol. 774, article 138768, 2020.

[9] F. Li, X. Ji, Z. X. Wu et al., "Digital light processing 3D printing of ceramic shell for precision casting," *Materials Letters*, vol. 276, article 128037, 2020.

[10] J. Guo, Y. Zeng, P. Li, and J. Chen, "Fine lattice structural titanium dioxide ceramic produced by DLP 3D printing," *Ceramics International*, vol. 45, no. 17, pp. 23007–23012, 2019.

[11] C. Esposito Corcione, F. Montagna, A. Greco, A. Licciulli, and A. Maffezzoli, "Free form fabrication of silica moulds for aluminium casting by stereolithography," *Rapid Prototyping Journal*, vol. 12, no. 4, pp. 184–188, 2006.

[12] T. An, K. T. Hwang, J. H. Kim, and J. Kim, "Extrusion-based 3D direct ink writing of NiZn-ferrite structures with viscoelastic ceramic suspension," *Ceramics International*, vol. 46, no. 5, pp. 6469–6476, 2020.

[13] D. A. Komissarenko, P. S. Sokolov, A. D. Evstigneeva et al., "DLP 3D printing of scandia-stabilized zirconia ceramics," *Journal of the European Ceramic Society*, vol. 41, no. 1, pp. 684–690, 2021.

[14] J. Zheng, H. Zhang, and X. Li, "Effect of ternary particles size distribution on rheology of slurry and microstructure of DLP printed ZTA ceramic," *Materials Chemistry and Physics*, vol. 269, article 124656, 2021.

[15] G. Zhang, J. Jiang, H. Wang, L. Qian, and H. Lan, "Continuous DLP-based ceramic 3D printing using a composite oxygen-rich film," *Journal of Manufacturing Processes*, vol. 64, no. 8, pp. 341–348, 2021.

[16] W. A. Sarwar, J. H. Kang, and H. I. Yoon, "Optimized zirconia 3D printing using digital light processing with continuous film supply and recyclable slurry system," *Materials*, vol. 14, no. 13, p. 3446, 2021.

[17] S. H. Yoo, H. C. No, H. M. Kim, and E. H. Lee, "Full-scope simulation of a dry storage cask using computational fluid dynamics," *Nuclear Engineering and Design*, vol. 240, no. 12, pp. 4111–4122, 2010.

[18] T. S. Zaripov, O. Rybdylova, and S. S. Sazhin, "A model for heating and evaporation of a droplet cloud and its implementation into ANSYS Fluent," *International Communications in Heat and Mass Transfer*, vol. 97, pp. 85–91, 2018.

[19] R. Ramesh Kumar and Y. Devarajan, "CFD simulation analysis of two-dimensional convergent-divergent nozzle," *International Journal of Ambient Energy*, vol. 41, no. 13, pp. 1505–1515, 2020.

[20] A. Moradi, D. Toghraie, A. Isfahani, and A. Hosseinian, "An experimental study on MWCNT–water nanofluids flow and heat transfer in double-pipe heat exchanger using porous media," *Journal of Thermal Analysis and Calorimetry*, vol. 137, no. 5, pp. 1797–1807, 2019.

[21] A. Rahimi Gheynani, O. Ali Akbari, M. Zarringhalam et al., "Investigating the effect of nanoparticles diameter on turbulent flow and heat transfer properties of non-Newtonian carboxymethyl cellulose/CuO fluid in a microtube," *International Journal of Numerical Methods for Heat and Fluid Flow*, vol. 29, no. 5, pp. 1699–1723, 2019.

[22] A. Yoshino, Y. Hotta, T. Hirozane, and M. Endo, "A numerical method for incompressible non-Newtonian fluid flows based on the lattice Boltzmann method," *Journal of Non-Newtonian Fluid Mechanics*, vol. 147, no. 1-2, pp. 69–78, 2007.

[23] J. Psihogios, M. E. Kainourgiakis, A. G. Yiotis, A. T. Papaioannou, and A. K. Stubos, "A lattice Boltzmann study of non-newtonian flow in digitally reconstructed porous domains," *Transport in Porous Media*, vol. 70, no. 2, pp. 279–292, 2007.

[24] G. Di Ilio, D. Chiappini, and G. Bella, "A comparison of numerical methods for non-Newtonian fluid flows in a sudden expansion," *International Journal of Modern Physics C*, vol. 27, no. 12, p. 1650139, 2016.

[25] M. Bisht and D. V. Patil, "Assessment of multiple relaxation time-lattice Boltzmann method framework for non-Newtonian fluid flow simulations," *European Journal of Mechanics B-Fluids*, vol. 85, pp. 322–334, 2021.

[26] M. Y. Gokhale and I. Fernandes, "Simulation of forced convection in non-Newtonian fluid through sandstones," *International Journal for Computational Methods in Engineering Science and Mechanics*, vol. 18, no. 6, pp. 302–308, 2017.

[27] D. Conrad, A. Schneider, and M. Bohle, "A viscosity adaption method for lattice Boltzmann simulations," *Journal of Computational Physics*, vol. 276, pp. 681–690, 2014.

[28] S. Gabbanelli, G. Drazer, and J. Koplik, "Lattice Boltzmann method for non-Newtonian (power-law) fluids," *Physical Review E Statistical Nonlinear & Soft Matter Physics*, vol. 72, no. 4, article 046312, 2005.

[29] W. Wu, X. Huang, C. Fang, and Y. Gao, "An improved MRT-LBM for Herschel–Bulkley fluids with high Reynolds number," *Numerical Heat Transfer Part B Fundamentals*, vol. 72, no. 6, pp. 409–420, 2017.

[30] S. Zou, X. F. Yuan, X. Yang, W. Yi, and X. Xu, "An integrated lattice Boltzmann and finite volume method for the simulation of viscoelastic fluid flows," *Journal of Non-Newtonian Fluid Mechanics*, vol. 211, pp. 99–113, 2014.

[31] D. G. Li, H. F. Zhang, P. X. Ye, and Z. Yu, "Natural convection of power-law nanofluid in a square enclosure with a circular cylinder: an immersed boundary-lattice Boltzmann study," *International Journal of Modern Physics C*, vol. 29, no. 11, article 1850105, 2018.

[32] Z. Guo, C. Zheng, and B. Shi, "Discrete lattice effects on the forcing term in the lattice Boltzmann method," *Physical Review E*, vol. 65, no. 4, article 046308, 2002.